Applied Physics B
Lasers and Optics

CrossMark

Nanostructured plasmas for enhanced gamma emission at relativistic laser interaction with solids

K. A. Ivanov[1,2] · D. A. Gozhev[1,2] · S. P. Rodichkina[1] · S. V. Makarov[3] · S. S. Makarov[1,4] · M. A. Dubatkov[1] ·
S. A. Pikuz[4,5] · D. E. Presnov[1] · A. A. Paskhalov[6] · N. V. Eremin[6] · A. V. Brantov[2] · V. Yu. Bychenkov[2] ·
R. V. Volkov[1] · V. Yu. Timoshenko[1,2,5] · S. I. Kudryashov[2,5] · A. B. Savel'ev[1]

Abstract The hot plasma formed onto the surface of nanostructured targets by a relativistically intense (up to 4×10^{18} W/cm^2), high contrast femtosecond laser radiation is studied. The nanoscale structures (pores, spheres, grass) were produced via laser ablation or chemical etching of bulk silicon and molybdenum. We report one of the first experimentally observed manifold enhancements of gamma yield at the background of hot electron energy growth from 200 to >600 keV, compared to the case of initially flat substrate in the relativistic regime of interaction. The efficiency of hot particle production is significantly affected by the shape of the structures. Experimental results are supported by 2D3V Particle-In-Cell simulations of laser–plasma interaction. It is shown that a laser-based plasma source, formed onto the surface of a solid target may be utilized for phase contrast X-ray imaging in a wide energy range of photons.

1 Introduction

The laser-driven plasma X-ray and gamma sources are of wide interest within the last decade. Their small size, high spatial coherence of the source, quasi-monochromaticity and ultra-short duration of the X-ray burst allows efficient use of laser–plasma for X-ray imaging with high spatial resolution (phase contrast imaging [1, 2]), gamma radiography [3–5], photonuclear reactions excitation [6, 7], etc. One of the main problems, hampering the vast integration of such sources, is the lack of luminosity in the hard X-ray range, compared to common synchrotron sources or even microfocus X-ray tubes, resulting in the necessity of long object exposure and the need to reproduce stable from shot to shot parameters of the plasma source at a high repetition rate within a series of a few hundreds or thousands pulses.

A solution to the issue may be found within the scope of two ways, which are, however, connected one to the other. The first implies the amplification of laser to plasma coupling with the use of micro- and nanostructured targets. Many groups have reported their remarkable results in this domain at moderate levels of laser intensities (10^{17} W/cm^2 and lower) [8–15]. Recent achievements in the target engineering and surface machining using chemical etching, controlled direct laser writing, 3D printing allow the formation of highly repeatable large area samples with different types of structures [10, 14, 16–19]. The second way is to increase the laser pulse intensity. Numerous PIC simulations of laser interaction with structures in the relativistic regime (when the peak laser intensity exceeds 10^{18} W/cm^2) revealed the efficient laser absorption and particle accelerations at sub-wavelength gratings, cones, nanowires, tubes, etc. [20–26].

Until the last few years, the experimental merging of these two directions into a fruitful conjunction was stuck mainly due to the problem of the laser pulse contrast, when

✉ K. A. Ivanov
akvonavi@gmail.com

1 Physics Faculty and International Laser Center of M.V. Lomonosov, Moscow State University, Leninskie gory 1, 119991 Moscow, Russia

2 P.N. Lebedev Physical Institute of Russian Academy of Sciences, Leninskiy Pr. 53, 119991 Moscow, Russia

3 ITMO University, Kronverksky Pr. 49, 197101 St. Petersburg, Russia

4 Joint Institute for High Temperatures of Russian Academy of Sciences, Izhorskaya st. 13/2, 125412 Moscow, Russia

5 National Research Nuclear University MEPhI, Kashirskoe Sh. 31, 115409 Moscow, Russia

6 Skobeltsyn Institute of Nuclear Physics of M.V. Lomonosov, Moscow State University, Leninskie gory 1, 119991 Moscow, Russia

the prepulses or pedestal of the main pulse destroys the structures and nullifies the advantages of the modified target because of preplasma formation. Only with the development of the contrast cleaning techniques (XPW and plasma mirror [27, 28]) the contrast ratio (i.e., the ratio between the normalized peak intensity of the main and the amplitude of the prepulse) was decreased to 10^{-10} and lower. Several groups reported their successful results on experimental enhancement of the plasma parameters utilizing nanograss (or nanorods) [24, 25], gratings [29], and carbon nanotubes [30] in the relativistic regime of laser-matter interaction.

In this paper, we present our recent results on the experimental comparison of the efficiency of gamma and hard X-ray generation at weakly relativistic high contrast femtosecond laser interaction with three different types of structured targets: nanoscale hemispheres onto the surface of a solid metal (Mo) target, nanoporous silicon and Si nanograss. We demonstrate that the targets exhibit an appreciable growth of hot electron temperature and high energy photon yield compared to their non-structured flat analog. The maximum increase is achieved for Si nanograss, where the recorded hot electron temperature grew up from ~200 to more than 600 keV, in comparison with flat Si substrate at the peak intensity of the femtosecond pulse up to 4×10^{18} W/cm^2. The size of the hot spot, emitting X-ray from the plasma, was measured to be ~13 μm FWHM using knife-edge technique. The possibility of X-ray phase contrast imaging registration of simple objects is demonstrated in the XUV range with limited exposure time; the formation of phase contrast images in hard X-ray range with reasonable geometry is discussed.

2 Experimental setup and target surfaces overview

In our experiments, the samples were placed inside a vacuum chamber and irradiated by tightly focused off-axis gold-coated parabola (F/D = 3) *p*-polarized femtosecond laser pulses at an angle of incidence of 45°. The radiation was delivered by a Ti:Sa laser system: $\lambda = 800$ nm, $\tau = 50$ fs, energy at target up to 30 mJ, repetition rate 10 Hz and peak-to-pedestal ratio $<10^{-9}$ (100 ps prior to main pulse). With the use of XPW contrast cleaner, the last could be achieved. The measurement of the energy distribution in the focal plane perpendicular to the beam axis by a microobjective revealed that diameter of the central spot was ~2.2 μm (FWHM), where ~30% of laser pulse energy was contained [31]. This provided the vacuum peak intensity up to 4×10^{18} W/cm^2.

For diagnosing the laser–plasma, we used two NaI scintillator gamma detectors to: i. control the high energy photon yield in each laser shot and ii. measure the gamma spectra

in the photon counting regime by collimating one of the device. Each spectrum was accumulated for ~10.000 shots with a counting rate of ~0.1–0.5 photon per pulse. After data processing with Monte-Carlo simulation of photon attenuation in matter we reconstructed the initial spectra of plasma and evaluated the hot electron temperature by fitting the tail of the exponentially decreasing distribution [32].

The lateral displacement of the target between each consequent shot was 100–300 microns to avoid irradiation of the residual crater and ablated area after the preceding laser pulse.

In total, five types of targets were regarded: a bulk flat Mo (see Fig. 1a) with a thickness of 2 mm and Si target, 550 μm thick, as reference points and three typical nanostructured targets: (i) ~100 nm nanosize hemi-spheres produced onto the surface of 2 mm thick Mo substrate, made by direct laser writing, Fig. 1b, (ii) Si nanopores, Fig. 1c, and Si nanograss, Fig. 1d, both made by chemical etching of 550 μm thick substrate. The silicon targets were glued onto the 2 mm Mo substrate to ensure the flatness during the irradiation and total absorption of fast electrons. Thus, we compared the efficiency of laser to plasma coupling for some characteristic modifications, which may be produced relatively easily.

Silicon nanostructures were produced by metal-assisted chemical etching (MACE) of lightly boron-doped (100)-oriented p-type c-Si [18]. To perform the method, c-Si wafers were at first rinsed HF(49%) for 1 min to remove the native oxide layer. Then, in the first step of MACE, surfaces of c-Si wafers were covered with Ag nanoparticles by immersing them in a mixture of aqueous solutions of HF (5 M) and $AgNO_3$ (0.002 or 0.02 M) at 1:1 ratio for 30 s. The higher concentration of $AgNO_3$ was used to produce arrays of Si nanograss, while the lower concentration allowed us to produce porous Si layers with pore sizes from 10 to 100 nm, i.e. Si nanopore samples. In the second step, the c-Si wafers covered by Ag nanoparticles were etched in a 10:1 solution of HF (5 M) and H_2O_2 (30%) for 1 h and then washed in deionized water. Finally, to remove Ag particles, the samples were placed in HNO_3 (65%) for 15 min and then washed in deionized water again.

The metal nanostructures were formed during femtosecond laser nanostructuring of the mechanically polished Mo surface. Its multipass raster-scanning under a 2-mm thick 2-propyl-alcohol layer was carried using a laser ablation workstation, equipped by an ytterbium-doped fiber laser system, the Satsuma (Amplitude Systems) with the following basic characteristics: central wavelength $\lambda \approx 1030$ nm, maximum energy $E_{max} \leq 10$ μJ in the TEM$_{00}$ mode, FWHM pulse width $\tau \approx 0.31$ ps, repetition rate $f = 0–2$ MHz, a galvanoscanner ATEKO™ and a 3D-motorized translation stage, all controlled by a PC. Laser pulses were focused by an antireflective silica glass objective (focal length ≈100 mm) of the galvanoscanner into a 12 μm wide (FWHM) spot on

Fig. 1 Scanning electron microscope images of structured targets: flat molybdenum (**a**) molybdenum nanospheres (**b**), silicon nanopores (**c**) and silicon nanograss (**d**)
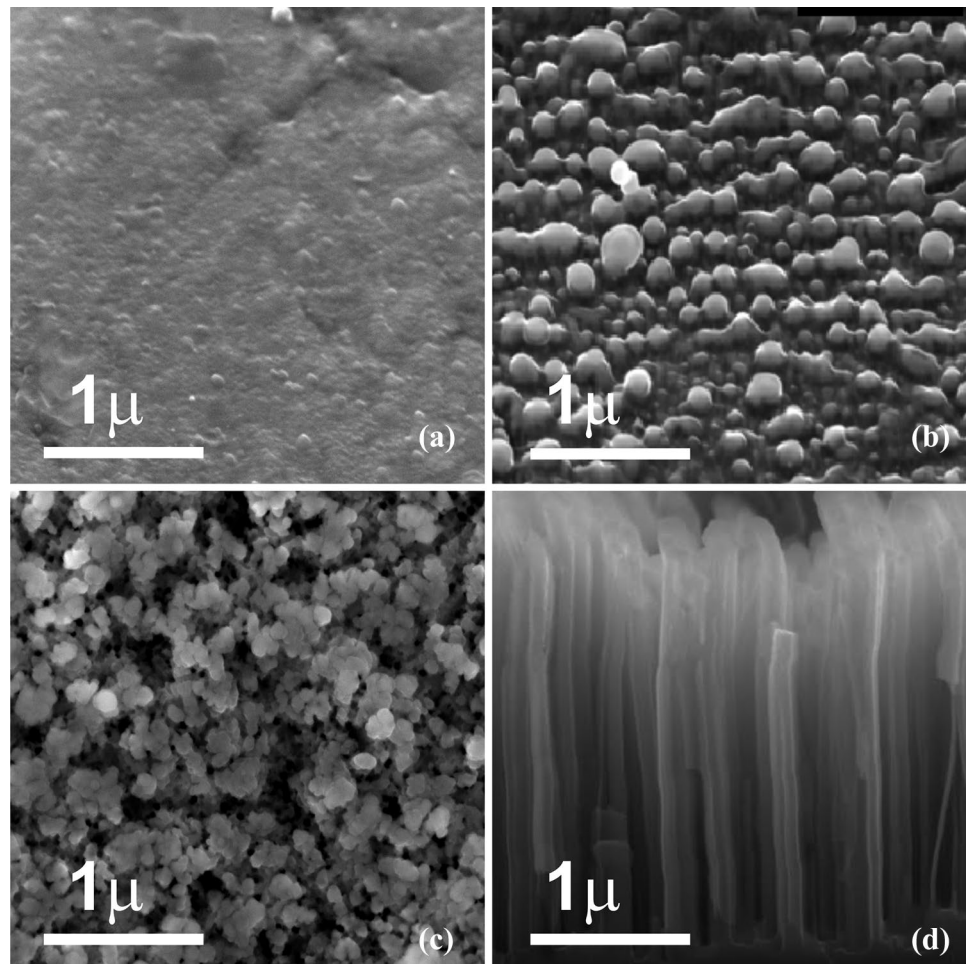
a sample surface (the peak laser fluence on the surface $F_0 \approx 3$ J/cm^2) and scanned across 5×5 mm^2 large area with 100-lines/mm filling at a scan velocity of 2 m/s and repetition rate of 500 kHz.

In principle, varying the parameters of the fabrication processes makes it possible to precisely control the density, shape, porosity, etc. of the formed structures. The laser-assisted method has its limitations concerning the height-to-diameter aspect ratio of the separate features (typically close to 1:1 or 2:1) [19]; however, it is more favorable for local periodicity due to diffraction and interference effects. Chemical etching leading to a random displacement of structures, is convenient for the growth of much taller structures (like nanograss, which can be up to hundreds of micrometers in height) along with their smaller thickness [18].

The resulting surface topographies were characterized by scanning electron microscopes JEOL JSM 7001 F and Zeiss Gemini SEM 300 (see Fig. 1).

The main advantages of the mentioned techniques for surface processing are the very high repeatability of pattern over the whole sample and ability to produce large area targets (tenths of square centimeters) for experiments at a high repetition rate. At the same time, the cost of the fabrication is low, which is very important.

In our previous letter [31] on this subject, we have demonstrated that the damage threshold for a structured surface is approximately one order of magnitude lower in terms of fluence than for an initially flat target. Hence the use of a high contrast laser pulse is necessary. Also because of this, the maximal intensity of the main pulse was retained below 5×10^{18} W/cm^2 to avoid destruction of nanomodifications before the main pulse arrival. It is worth mentioning that the front of the pulse is still able to form a short preplasma; however, the expansion rate does not acquire catastrophic consequences due to short picosecond scale delay between the prepulses and the main pulse.

3 Main experimental results

Accumulating and then processing data we observed two different results. At first, it should be noted, that for each type of structured target the increase of gamma and hard X-ray yield was detected (though different for any kind of target)

in comparison with an initially flat substrate. However, for Si nanopores this was the only observed effect. Whereas for molybdenum nanospheres and for silicon nanowires, we also measured a huge raise in hot electron temperature.

Both for flat Mo and Si, the hot electron temperature was around 150–200 keV (see Fig. 2). In experiments with Mo target, the peak intensity was ~2×10^{18} W/cm^2, whereas for Si targets it was ~4×10^{18} W/cm^2. The estimated temperature is slightly lower than the one expected from ponderomotive scaling (typical for this range of intensity) [33]. This discrepancy may be attributed to the high optical reflectivity of polished Mo and Si substrate and high contrast, resulting in a sharp plasma-vacuum interface. The cutoff in each spectrum at low energy is explained by the thick metal plate (a few millimeters of lead) to filter the flux of low energy photons.

Analysis of the spectra of silicon nanopores revealed that photon yield with energy above 200 keV increased three times with similar hot electron temperature (~200 keV) as compared to a flat silicon substrate. The measured conversion efficiency into gammas (>300 keV) was ~3×10^{-6}% for nanopores. We assume that due to a significantly enhanced

surface of interaction the laser pulse was absorbed with higher efficiency. At the same time the non-uniformity of the modifications, along with their aperiodicity, does not contribute to the local electro-magnetic field amplification or plasmon effects [14, 23, 29], which could result in an increased hot electron temperature. The enhancement of hot electron production at interaction with nanopores was demonstrated theoretically and experimentally previously in our group, though at a lower peak intensity level [11, 34]. Increased absorption of laser radiation and electron energy gain were related to the high porosity and local irregularity of the electric field at the pores edges. Enhancement of soft X-ray emission at moderate intensity interaction was also reported by Nishikawa et al. [9]. Authors indicated the role of small preplasma in the efficiency of X-ray generation. Since the contrast of our laser pulse is high but still limited, the pre-ionization of the surface may also play a role in this case.

The hot electron temperatures evaluated from the spectra of molybdenum nanospheres and silicon nanowires were ~500 and 630 keV correspondingly, which is more than thrice higher than for initially flat Mo and Si (see Fig. 2). The hard X-ray yield increased almost one order of magnitude at the same conditions when irradiating nanowires. The conversion efficiency reached almost 10^{-5}% in the gamma range (above 500 keV). For Mo nanospheres, the laser energy conversion was lower - ~5×10^{-6}% in the same energy range. We believe that here a mechanism different from the ponderomotive heating of hot electron production began to play a role, though this mechanism is not the same for nanospheres and nanowires.

At the interaction with more or less periodically placed Mo nanospheres, the acceleration of hot particles may be attributed to several phenomena: Mie resonance, vacuum heating or stochastic heating. These effects were already discussed with respect to the irradiation of sub-wavelength spheres [20, 35, 36]. A simple formula for effective rescaled intensity at interaction with a wavelength-size sphere was derived by Rajeev et al. [35]: $I_r = I_{in}((L_\perp^{surf})^2 \sin^2\theta + \cos^2\theta)$, where I_{in} is the vacuum intensity, $L_\perp^{surf}$ is the local field correction factor (typically ~3 for a spherical particle) and θ is the angle of laser incidence. At our conditions the intensity growth factor was ~5. Considering the scaling for ponderomotive acceleration, the hot electron temperature of ~500 keV would be achieved, which is quite close to the measured value. However, the diameter of the spheres may also play a significant role. It is worth mentioning that in this paper the optimal diameter of the spheres was close to λ. The initial size of the molybdenum spheres in our experiment was lower (~100 nm). Hence the slight expansion of the nanomodifications by the action of the prepulses, or the front of the main pulse, may be present. Nevertheless, the contrast of the pulse must be retained low enough to avoid
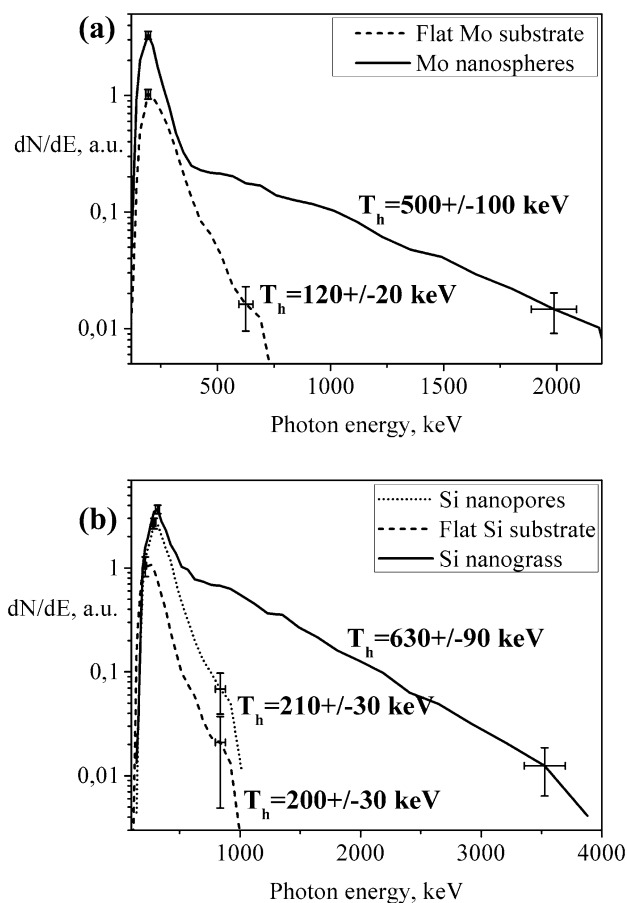
Fig. 2 Gamma spectra for different types of target: molybdenum substrate and nanospheres (**a**) and silicon substrate, nanopores and nanograss (**b**)

total destruction of the nanomodifications and disappearance of the structured surface effects [37].

Taking into account the exponential form of the gamma spectra, we assume that the growth of photon emission is expected also for the low energy part of spectra (near K-edge of molybdenum). This permits us to introduce the source for varied application (X-ray absorption, phase contrast imaging, etc.).

The interaction of a high intensity laser pulse with silicon nanowires or nanograss at normal incidence is often accompanied by a deep penetration of the laser field into the target due to guiding and low average density [25] increasing the overall light absorption. Simultaneously the particles, trapped by the field of the pulse, may undergo multiple get-outs from the laser phase through propagation for nontransparency in light silicon rods, and hence efficiently gain energy through ponderomotive action when re-emerging from the other side of the rod. However, the electron energy gain mechanisms are strongly dependent on peak laser fluence and may be different for moderate [10, 14] and relativistic ranges of intensity [25]. Our regime of a slightly relativistic laser action may involve several effects. Moreover, the laser is not normally incident onto the nanorods, which may result in additional peculiarities of interaction.

To our knowledge, such huge growth both of gamma, hard X-ray yield and hot electron temperature at over 10^{18} W/cm^2 intensity is one of the first to be observed in experimental literature utilizing nanostructured targets. This approach will be developed and new target structures will be investigated soon.

4 Particle-in-cell modeling

For a better understanding of the hot electron generation mechanism at the surface of a nanograss target, we performed a PIC modeling of the laser interaction with nanorods. In the fully relativistic 3D3V code MANDOR [38] (here 2D simulations were performed), we modeled a box 16×16 microns with a resolution of 5 nm. The 50 fs FWHM laser pulse with a wavelength of 1 μm was focused into a 4 μm spot to peak intensity 2×10^{18} W/cm^2. A flat foil tilted at 45 degrees to the beam axis was placed in the focal region. The density of the foil was 5 N_{cr}, the thickness 1 μm. To simulate the action of the prepulses, a short preplasma with an exponential decay starting at $N_e = N_{cr}$ and characteristic scale length $L/\lambda = 0.1$ was placed in front of the foil. The nanorods with a diameter of 200 nm, length of 5 μm and density of 5 N_{cr}, placed onto the flat foil at a random distance one from the other in a range from 50 to 200 nm, were additionally encountered by a short preplasma (100 nm, with a linear ramp from 0 to 0.1 N_{cr}), see Fig. 3a. We also modeled
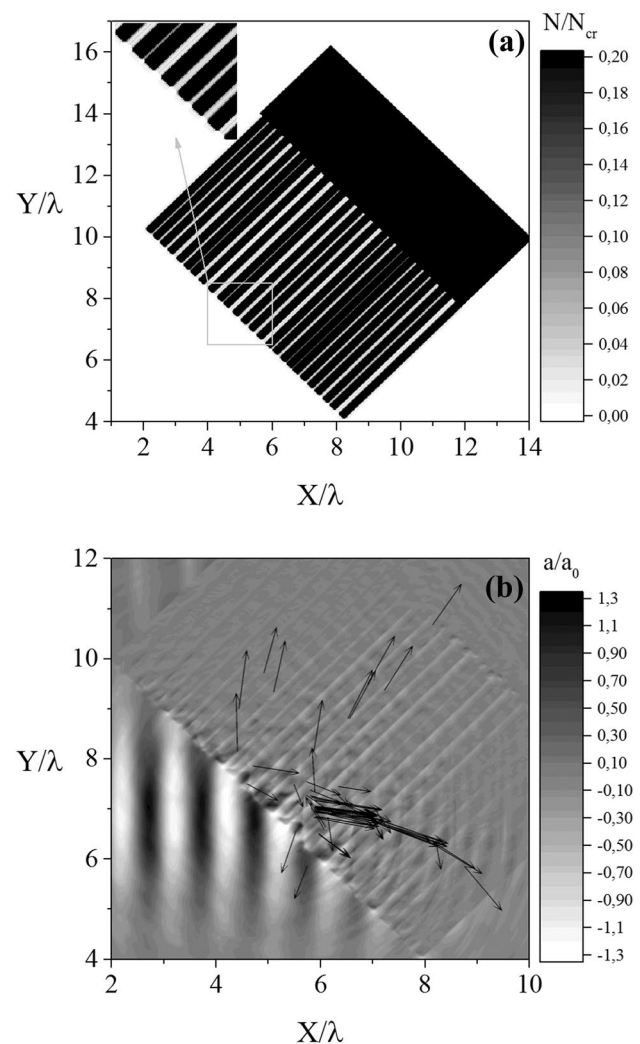
Fig. 3 **a** Initial electron density distribution in the simulation box modeling the nanograss target with rods length 5 μm. **b** Electric field distribution in units of dimension less amplitude a_0 in the simulated area 105 fs after beginning of computation. The black arrows indicate the position and momentum direction of some of the electrons with energy above 1.5 MeV

the interaction of radiation with 1 μm length nanorods. The temporal resolution was 10^{-3} fs.

A brief analysis of the electric field in the simulation box for nanowires with a length of 5 μm (at the moment, when the particles with highest momentum are generated, see Fig. 3b) shows, that the electrons are expelled from the top of the nanorods by the field, resulting in the propagation of the laser pulse deeper in between the structures. However, due to small spacing between the wires (much less than the wavelength) and large angle of incidence the laser pulse did not penetrate deeper than ~1 μm. Moreover, the propagation of laser radiation is hampered by the blurring of the rods. For these reasons, no substantial difference in modeling for 1 or 5 μm nanorods was observed.

The fast electrons are accelerated just at a depth of approximately one micron in the complex field of incident and reflected laser waves and the Coulomb field of positively charged rods. One may observe two groups of fast particles, Fig. 3b: the first penetrates into the bulk of the target, and the second one, much more numerous, is propagating almost along the surface of the target.

Analyzing the spectra of electrons in the simulation box, we detected substantial growth of a quantity of high energy particles (almost one order of magnitude for particles with energy above 500 keV) and their maximal energy (up to 2 MeV and higher), compared to the flat target, see Fig. 4.

It is worth mention that almost all the fast particles penetrate into the target, contributing to the generation of gamma and hard X-rays. This situation is more favorable in this aspect, compared to a flat target, when due to mechanisms of hot electron generation in the preplasma, the particles with high momentum are accelerated and expelled along the direction of reflected from the surface laser radiation [39].

The PIC result is reasonably close to the experimental one (since the bremsstrahlung spectrum reproduces the electron distribution well [40]). However, it is noteworthy that the simulation results may be dependent on parameters (peak intensity, rods displacement, etc.) Without pretending to a strict reproduction of the target structure and parameters in the modeling we suppose, however, that the result is quite representative, and our calculations show the principled opportunity of particle acceleration by the penetrating into the nanorods electric field of laser radiation.
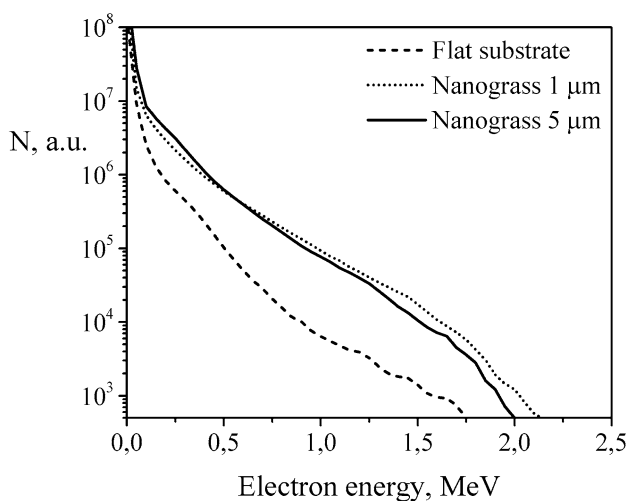
**Fig. 4** Electron energy spectra for flat foil and nanowires target with different rods length

5 Discussion and applications

Being able to significantly increase the laser to plasma coupling with the use of the above-mentioned types of nanostructured target, it is possible to talk about some applications which may be realized with such an X-ray source. Both molybdenum and silicon have bright K-edge linear radiation in the keV range (17.5 and 1.74 keV correspondingly), suitable for X-ray imaging with high spatial resolution, densitometry, X-ray absorption spectroscopy, and investigation of fast processes, since the duration of the X-ray burst is within several picoseconds [3–5]. At the moment the brightness of the laser-driven sources is low, compared to synchrotron radiation sources, to perform single shot diagnostics. However, with the target production techniques available we are able to create large area sample (tenths of cm^2).

For the flat molybdenum target we made a simple experiment by exposing a nickel grid (~ 100 μm wide and ~ 50 μm thick) to the plasma radiation. The source to object (SO) distance was 13 cm. A LiF crystal, placed at an object to detector (OD) distance of 13 cm as well, registered the image through formation of color centers in the crystal under the action of high energy photons [2, 41, 42]. The exposure time was 1000 laser shots. Both the object and the detector were placed in a vacuum chamber in front of the target.

After developing the crystal near the surface layer on a scanning luminescent microscope Zeiss LSM 700 Confocal, the image of the metal grid was obtained, see Fig. 5a. The analysis of the profile of the grid allowed us to estimate the spatial size of the source at first (through the transition from dark to bright regions since the edge of the grid acted like a knife for source size estimation), and to reveal the formation of phase contrast at the second (through the interferometric fringes at the same grid edge), see Fig. 5b. The estimate by this technique source size was 15 ± 5 μm, and the level of contrast (which is estimated as the ratio of maximal and minimal intensities to their sum) achieves 20% at the grid edge. However, it should be noted that the photons' flux, forming the image on the crystal, consists mainly of relatively low energy quanta (0.1–1 keV), which are efficiently absorbed in the thin surface layer which has been analyzed by the microscope. The hot spot size in a higher energy range (a few keV or around K_α line) may be different (up to a few tenths of microns in diameter [43]), though it is still applicable for phase contrast imaging.

To graphically illustrate the phase contrast formation at the grid edge we performed numerical calculations of the Fresnel-Kirchhoff integral for diffraction of X-ray waves similar to the experiment geometry: a linear set of 15 point-like sources were placed at a distance of 1 μm one from each other; the source to object and object to detector distance were taken 13 cm. At the detector plane the resulting image was formed by the incoherent sum of each point source.

(a)

(b)
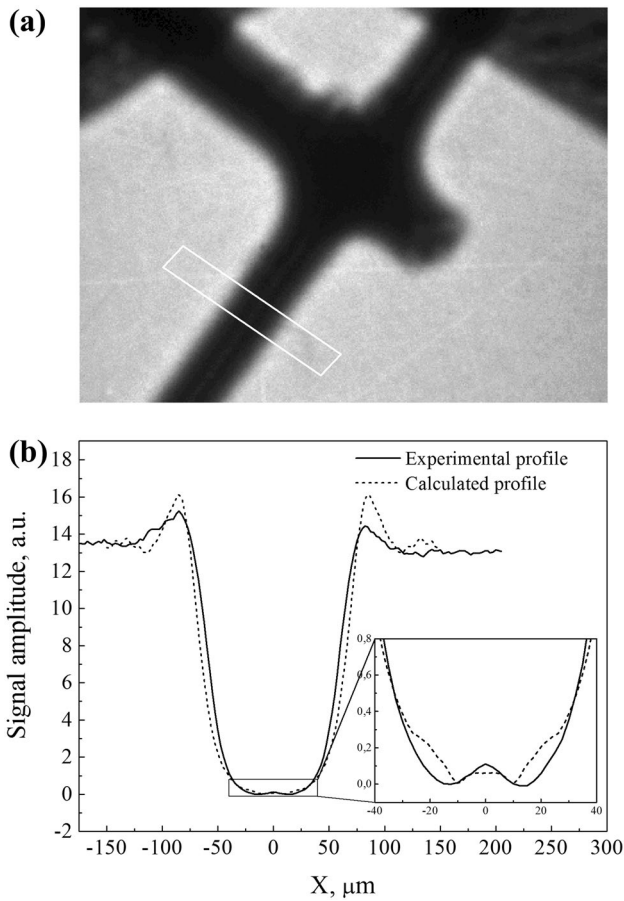
Fig. 5 **a** Developed image of LiF crystal surface with a shadow from the metal grid. **b** Experimental profile of the edge of the metal wire (the white rectangle in **a** illustrates the region, over which the profile of the grid was measured) and numerically calculated profile with similar conditions of exposure (see text for details)

Since the wavelengths forming the images are not known exactly, we varied them in the calculation. With photons at wavelengths of 1–10 nm (or ~0.1–1 keV, uniform spectral intensities of different wavelengths), we obtained a reasonable agreement between the experiment and the numerical calculations, see Fig. 5b: the contrast level achieves 20% at the edge; we could also elucidate the intensity hop in the center of the wire—a typical manifestation of the diffraction effect.

Along with gamma spectra, the few keV range photon distributions were measured at the irradiation of flat molybdenum by a Greenstar X-ray detector equipped with an Amptek SiPIN diode, Fig. 6. After elaboration, the flux of K_α Mo photons (~17 keV) reached $(7 \pm 1) \times 10^7$ per pulse in 4π sr, or ~10^{-3}% of laser pulse energy. This value is in good agreement with the results of other groups utilizing Mo as a target material [1].

To elucidate the phase contrast formation with high energy photons, we calculated the diffraction of X-ray waves
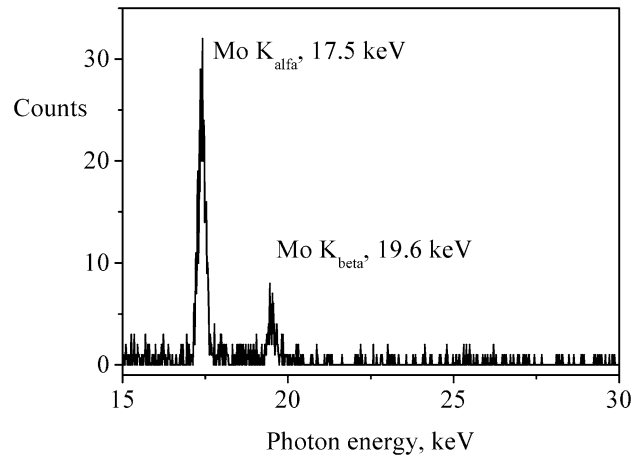
Fig. 6 X-ray spectrum of flat Mo target, measured by X-ray SiPIN detector

on the edge of a thin (7 μm) mylar foil. For this we modeled the experimental spectrum of the Mo source (see Fig. 6): the central line around 17 keV, or K_α line of Mo, was encountered by a number of lines with energy from 10 to 25 keV with spectral intensity 1% of the main line. By varying the source to object (SO) and object to detector (OD) distances we found that a contrast level over 20% may be achieved, see Fig. 7. It is worth mentioning that this allows for the investigation of objects with low density variations, which are unattainable for conventional X-ray techniques. The SO and OD may be retained within 50 cm, thus preserving relatively high photon flux on the object. The width of the
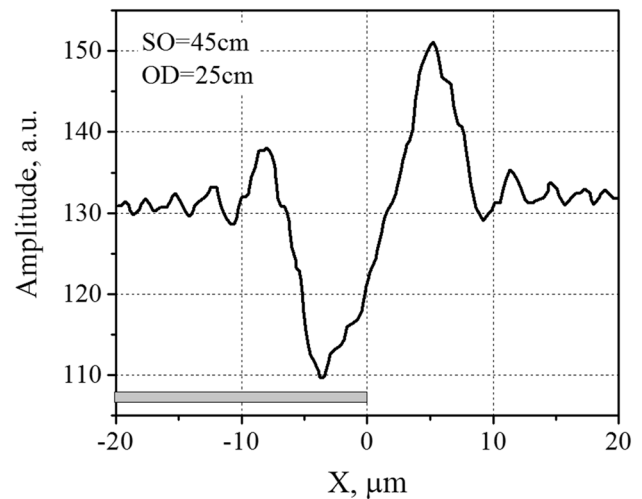
Fig. 7 Phase contrast formation on the detector plane from the edge of 7 μm mylar foil (with the edge at $X = 0$ μm), exposed to photons with spectral distribution, measured for Mo target (see Fig. 6 and text for details). The source to object SO and object to detector OD distances are 45 and 25 cm correspondingly. The gray rectangle illustrates the position of the foil relative to the horizontal axis

interferometric fringe on the detector plane (>10 μm) allows the use of direct X-ray detectors with pixel size ~5 μm and almost 100% efficiency around 10 keV.

6 Conclusions

To summarize, at relativistic regime of high contrast (<10^{-9} 100 picoseconds prior to main pulse) femtosecond laser interaction (over 10^{18} W/cm^2) with typical nanostructured targets (nanopores, nanospheres and nanograss), produced by laser ablation and chemical etching of solids, the substantial growth of gamma as well as hard X-ray emission (up to tenfold) may be achieved in comparison with flat target irradiation. Such a huge increase is one of the first to be experimentally demonstrated. The hot electron temperature rose from 200 keV (for initially flat bulk target) to up to 630 keV (at irradiation of a nanograss target with a typical rod thickness of ~100–200 nm and similar distance from one to the other, and length of ~3 μm). The highest conversion efficiency into the gamma range (>500 keV) was detected by irradiating silicon nanowires, and was estimated on the level of 10^{-5}%. Silicon nanopores and molybdenum nanospheres revealed a lower conversion of laser energy into gamma rays, though still increased three to five times if compared to flat substrate.

At the same time, the growth of spectra efficient temperature (i.e., the hot electron temperature) is measured for nanospheres and nanograss, whereas the interaction with pores reveals only enhanced X-ray emission, indicating the amplified laser absorption was due to the developed surface of the target, not the efficient acceleration of particles in the complex laser field.

The experimental results are supported by PIC modeling of intense laser action onto nanograss, showing significant increase of hot electron production and energy gain due to efficient acceleration of the particles along the rods by the penetrated field of the laser pulse.

We have demonstrated that the source, formed onto the surface of solid bulk target, may be utilized for phase contrast image formation of simple objects. The contrast level of ~20% was achieved when exposing a thin metal wire to photons with energy in the 0.1–1 keV range. The measured size of the plasma source is ~13 μm. Our calculations have shown that the plasma source may be efficiently used for image formation also at a higher energy range (up to tenths of keV) with low exposure time.

References

1. R. Toth, S. Fourmaux, T. Ozaki, M. Servol, J.C. Kieffer, R.E. Kincaid, A. Krol, Phys. Plasmas **14**, 053506 (2007)
2. S.V. Gasilov, A.Y. Faenov, T.A. Pikuz, I.Y. Skobelev, F. Calegari, C. Vozzi, M. Nisoli, G. Sansone, G. Valentini, S. De Silvestri, S. Stagira, JETP Lett. **87**, 238 (2008)
3. R.D. Edwards, M.A. Sinclair, T.J. Goldsack, K. Krushelnick, F.N. Beg, E.L. Clark, A.E. Dangor, Z. Najmudin, M. Tatarakis, B. Walton, M. Zepf, K.W.D. Ledingham, I. Spencer, P.A. Norreys, R.J. Clarke, R. Kodama, Y. Toyama, M. Tampo, Appl. Phys. Lett. **80**, 2129 (2002)
4. K.T. Phuoc, S. Corde, C. Thaury, V. Malka, A. Tafzi, J.P. Goddet, R.C. Shah, S. Sebban, A. Rousse, Nat. Photonics **6**, 308 (2012)
5. H.-P. Schlenvoigt, K. Haupt, A. Debus, F. Budde, O. Jäckel, S. Pfotenhauer, H. Schwoerer, E. Rohwer, J.G. Gallacher, E. Brunetti, R.P. Shanks, S.M. Wiggins, D.A. Jaroszynski, Nat. Phys. **4**, 130 (2007)
6. K. Ledingham, I. Spencer, T. McCanny, R. Singhal, M. Santala, E. Clark, I. Watts, F. Beg, M. Zepf, K. Krushelnick, M. Tatarakis, A. Dangor, P. Norreys, R. Allott, D. Neely, R. Clark, A. Machacek, J. Wark, A. Cresswell, D. Sanderson, J. Magill, Phys. Rev. Lett. **84**, 899 (2000)
7. D. Umstadter, J. Phys. D Appl. Phys. **36**, R151 (2003)
8. A.V. Ovchinnikov, O.F. Kostenko, O.V. Chefonov, O.N. Rosmej, N.E. Andreev, M.B. Agranat, J.L. Duan, J. Liu, V.E. Fortov, Laser Part. Beams **29**, 249 (2011)
9. T. Nishikawa, H. Nakano, H. Ahn, N. Uesugi, T. Serikawa, Appl. Phys. Lett. **70**, 1653 (1997)
10. G. Kulcsar, D. AlMawlawi, F. Budnik, P. Herman, M. Moskovits, L. Zhao, R. Marjoribanks, Phys. Rev. Lett. **84**, 5149 (2000)
11. R.V. Volkov, V.M. Gordienko, M.S. Dzhidzhoev, B.V. Kamenev, P.K. Kashkarov, Y.V. Ponomarev, A.B. Savel'ev, V.Y. Timoshenko, A.A. Shashkov, Quantum Electron. **25**, 192 (1998)
12. S.A. Gavrilov, D.M. Golishnikov, V.M. Gordienko, A.B. Savel'ev, R.V. Volkov, Laser Part. Beams **22**, 301 (2004)
13. S. Chaurasia, D.S. Munda, P. Ayyub, N. Kulkarni, N.K. Gupta, L.J. Dhareshwar, Laser Part. Beams **26**, 473 (2008)
14. S. Mondal, I. Chakraborty, S. Ahmad, D. Carvalho, P. Singh, A.D. Lad, V. Narayanan, P. Ayyub, G.R. Kumar, J. Zheng, Z.M. Sheng, Phys. Rev. B **83**, 35408 (2011)
15. U. Chakravarty, V. Arora, P.A. Naik, J.A. Chakera, H. Srivastava, A. Srivastava, G.D. Varma, S.R. Kumbhare, P.D. Gupta, J. Appl. Phys. **112**, 053301 (2012)
16. E.V. Golosov, A.A. Ionin, Y.R. Kolobov, S.I. Kudryashov, A.E. Ligachev, S.V. Makarov, Y.N. Novoselov, L.V. Seleznev, D.V. Sinitsyn, A.R. Sharipov, Phys. Rev. B **83**, 115426 (2011)
17. J. Fischer, M. Wegener, Laser Photonics Rev. **7**, 22 (2013)
18. V.A. Georgobiani, K.A. Gonchar, L.A. Osminkina, V Yu. Timoshenko, Semiconductors **49**, 1025 (2015)
19. A.A. Ionin, S.I. Kudryashov, A.O. Levchenko, S.V. Makarov, I.N. Saraeva, A.A. Rudenko, A.V. Butsen, V.S. Burakov, JETP Lett. **106**, 247 (2017). **(in Russian, to be published in English soon)**
20. O. Klimo, J. Psikal, J. Limpouch, J. Proska, F. Novotny, T. Ceccotti, V. Floquet, S. Kawata, New J. Phys. **13**, 053028 (2011)
21. M.A. Purvis, V.N. Shlyaptsev, R. Hollinger, C. Bargsten, A. Pukhov, A. Prieto, Y. Wang, B.M. Luther, L. Yin, S. Wang, J.J. Rocca, Nat. Photonics **7**, 796 (2013)
22. A. Andreev, N. Kumar, K. Platonov, A. Pukhov, Phys. Plasmas **18**, 103103 (2011)

23. A. Andreev, K. Platonov, J. Braenzel, A. Lübcke, S. Das, H. Messaoudi, R. Grunwald, C. Gray, E. McGlynn, M. Schnürer, Plasma Phys. Control. Fusion **58**, 14038 (2016)
24. L.L. Ji, J. Snyder, A. Pukhov, R.R. Freeman, K.U. Akli, Sci. Rep. **6**, 23256 (2015)
25. S. Jiang, L.L. Ji, H. Audesirk, K.M. George, J. Snyder, A. Krygier, P. Poole, C. Willis, R. Daskalova, E. Chowdhury, N.S. Lewis, D.W. Schumacher, A. Pukhov, R.R. Freeman, K.U. Akli, Phys. Rev. Lett. **116**, 085002 (2016)
26. A.V. Brantov, VYu. Bychenkov, Contrib. Plasma Phys. **53**, 731 (2013)
27. A. Jullien, S. Kourtev, O. Albert, G. Chériaux, J. Etchepare, N. Minkovski, S.M. Saltiel, Appl. Phys. B **84**, 409 (2006)
28. B. Dromey, S. Kar, M. Zepf, P. Foster, Rev. Sci. Instrum. **75**, 645 (2004)
29. A. Sgattoni, L. Fedeli, G. Cantono, T. Ceccotti, A. Macchi, Plasma Phys. Control. Fusion **58**, 14004 (2016)
30. H. Habara, S. Honda, M. Katayama, H. Sakagami, K. Nagai, K.A. Tanaka, Phys. Plasmas **23**, 63105 (2016)
31. K.A. Ivanov, A.V. Brantov, S.I. Kudryashov, S.V. Makarov, D.A. Gozhev, R.V. Volkov, A.A. Ionin, VYu. Bychenkov, A.B. Savel'ev, Laser Phys. Lett. **12**, 46005 (2015)
32. K.A. Ivanov, S.A. Shulyapov, P.A. Ksenofontov, I.N. Tsymbalov, R.V. Volkov, A.B. Savel'ev, A.V. Brantov, VYu. Bychenkov, A.A. Turinge, A.M. Lapik, A.V. Rusakov, R.M. Djilkibaev, V.G. Nedorezov, Phys. Plasmas **21**, 093110 (2014)
33. G. Malka, J. Miquel, Phys. Rev. Lett. **77**, 75 (1996)
34. YuM Mikhailova, V.T. Platonenko, A.B. Savel'ev, Quantum Electron. **35**, 38 (2005)
35. P. Rajeev, P. Taneja, P. Ayyub, A. Sandhu, G. Kumar, Phys. Rev. Lett. **90**, 115002 (2003)
36. H.A. Sumeruk, S. Kneip, D.R. Symes, I.V. Churina, A.V. Belolipetski, G. Dyer, J. Landry, G. Bansal, A. Bernstein, T.D. Donnelly, A. Karmakar, A. Pukhov, T. Ditmire, Phys. Plasmas **14**, 062704 (2007)
37. P.P. Rajeev, S. Kahaly, S. Bagchi, S. Bose, P.P. Kiran, P. Ayyub, G.R. Kumar, J. Phys. IV **133**, 533 (2006)
38. D.V. Romanov, VYu. Bychenkov, W. Rozmus, C.E. Capjack, R. Fedosejevs, Phys. Rev. Lett. **93**, 215004 (2004)
39. K.A. Ivanov, I.N. Tsymbalov, S.A. Shulyapov, D.A. Krestovskikhm, A.V. Brantov, VYu. Bychenkov, R.V. Volkov, A.B. Savel'ev, Phys. Plasmas **24**, 063109 (2017)
40. K.A. Ivanov, S.A. Shulyapov, A.A. Turinge, A.V. Brantov, D.S. Uryupina, R.V. Volkov, A.V. Rusakov, R.M. Djilkibaev, V.G. Nedorezov, VYu. Bychenkov, A.B. Savel'ev, Contrib. Plasma Phys. **53**, 116 (2013)
41. A. Ustione, A. Cricenti, F. Bonfigli, F. Floar, A. Lai, T. Marolom, R.M. Montereali, G. Baldacchini, A. Faenov, T. Pikuz, L. Reale, Appl. Phys. Lett. **88**, 141107 (2006)
42. T. Pikuz, A. Faenov, T. Matsuoka, S. Matsuyama, K. Yamauchi, N. Ozaki, B. Albertazzi, Y. Inubushi, M. Yabashi, K. Tono, Y. Sato, H. Yumoto, H. Ohashi, S. Pikuz, A.N. Grum-Grzhimailo, M. Nishikino, T. Kawachi, T. Ishikawa, R. Kodama, Sci. Rep. **5**, 17713 (2015)
43. G. Pretzler, Th Schlegel, E. Fill, D. Eder, Phys. Rev. E **62**, 5618 (2000)